# Fast and Secure Operation of Voltage Source Inverter based DERs using Model Predictive Droop Control

Waleed Alhosaini
Department of Electrical Engineering
University of Arkansas
Fayetteville, Arkansas
wsalhosa@uark.edu

Mohammad Hazzaz Mahmud
Department of Electrical Engineering
University of Arkansas
Fayetteville, Arkansas
mhmahmud@uark.edu

Yue Zhao

Department of Electrical Engineering

University of Arkansas

Fayetteville, Arkansas

yuezhao@uark.edu

Abstract— Reliability of the power grid can be improved by the use of microgrids (MGs) concept, which regulates the voltage and frequency at the point of common coupling (PCC) during normal and/or faulty conditions. Droop characteristics based hierarchical control strategies are commonly used in MGs, where power converters can operate in parallel. However, the need of multiple control loops not only adds complexity to the controller design, but also reduces the dynamic response of the system. In the future power system, grid-tied converters with fast dynamic response are desired to handle the uncertainties induced by high penetration of distributed energy resources. Therefore, this paper presents a novel model predictive control to ensure fast dynamic response of high power three-level converters in stand-alone operating mode as well as grid-tied operating mode. The proposed controller is applied to a MG which consists of a solar inverter connected in parallel with an energy storage system to the PCC, where a local load is tied. Both simulation and experimental results are presented to demonstrate robustness and the high dynamic performance of the proposed controller under rapidly changing atmospheric conditions and different grid operating modes.

Keywords—droop control, energy storage system, microgrid, model predictive control

## I. INTRODUCTION

The penetration level of distributed energy resources (DERs), especially the photovoltaic (PV) systems, in the power grid has been significantly increased over the last decade [1], [2]. The grid integration of DERs has brought various benefits, including energy savings, reduced system losses, deferred or avoided system investments, and improved power quality. However, the reliability and stability of the power grid might be negatively affected, if improper control approaches are used [3]-[5]. To mitigate these issues, various control strategies have been developed for MGs, which may consist of PV systems, ESSs and local loads.

One of the common MG control methods is the droop control, also known as autonomous control. The droop control strategy is widely adopted in MGs to regulate the voltage and frequency at the point of common coupling (PCC) during normal grid operation and under fault events. One of the main advantages of using droop control is that the communication is dispensable, since it only depends on local measurements. Thus, droop control improves the system reliability [3]-[5]. However, the droop control also presents several drawbacks. Firstly, the existence of the multiple control loops in droop control leads to have slow dynamic response. Secondly, the

system stability is highly affected by the selection of droop gains [6].

Recently, due to its robustness and fast dynamic response, model predictive control (MPC) has been applied to various power electronics applications, including grid-tied converters, active filters, motor drives, etc., [7]-[10]. Unlike the classic linear control methods used in autonomous control, applying MPC along with droop control should help decouple the interdependent control loops and eventually enhance the dynamic response. In this work, a novel model predictive droop control (MPDC) approach is proposed to ensure fast and robust operation of DERs. To design the MPDC, firstly, the discrete-time models for the converters and the associated filters are derived. Then, these discrete-time models are utilized for the prediction of DERs' future behavior. Finally, the switching states which minimizes the proper designed cost function is selected and to be applied in the next control cycle [6]-[10].

In this work, both simulation and experimental studies are performed to demonstrate that the proposed control strategy has fast dynamic response and robustness against the extreme change in solar irradiance regardless the converters' operating modes. The national MG studied in this work consists of a utility-scale solar inverter, a grid-tied ESS converter and a local load connected to the PCC. A circuit breaker (CB) is used to connect and disconnect the MG to the main power grid as it is shown in Fig. 1.

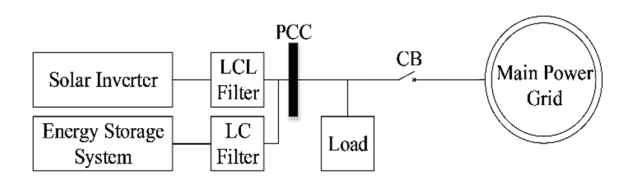


Fig.1. One-line diagram of MG studied in this work

#### II. SYSTEM MODELING

In this work, the three-phase three-level neutral point clamped (NPC) converters are used to link both the solar generation and ESS to the PCC. An *LCL* filter is designed to eliminate the harmonics introduced by the solar inverter, while an *LC* filter is designed to connect the battery ESS to the PCC. The design and implementation of MPDC requires the discrete-time mathematical models of the aforementioned systems. As a result, the models of the NPC inverters, the dclink, both *LCL* filter and *LC* filter are presented in this section.

This work was supported in part by the U.S. National Science Foundation (NSF) within the Industry/University Cooperative Research Center (I/UCRC) on Grid Connected Advanced Power Electronic Systems (GRAPES) under Grant IIP-1439700.

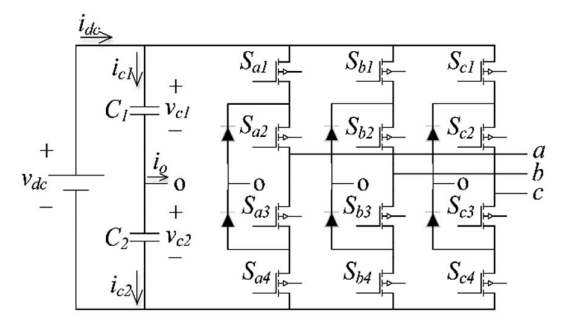


Fig. 2. The schematic of an NPC inverter

## A. NPC Converter Model

The circuit topology of a three-phase NPC inverter is shown in Fig. 2. In this NPC converter, 19 different active voltage space vectors can be produced as a result of all the 27 possible switching states. These voltage space vectors [11], [12], can be determined by using

$$v_{cnv} = \frac{2}{3}(v_{ao} + a \cdot v_{bo} + a^2 \cdot v_{co})$$
 (1)

where

$$v_{ao}$$
,  $v_{bo}$  and  $v_{co}$  inverter's output voltages;  $a$   $e^{j2\pi/3}$ .

Assuming balanced voltage across the two capacitors, i.e.,  $v_{c1} = v_{c2}$ , the NPC inverter's terminal voltages [11], [12], can be expressed as

$$v_{xo} = S_x \frac{V_{dc}}{2} \tag{2}$$

where  $V_{dc} = v_{c1} + v_{c2}$  and  $x = \{a, b, c\}$ 

The switching state of phase x is determined by the switching variable  $S_x$ . Only three switching values can be selected for the NPC converter which are +, 0, and -. Each one of these possible values leads to the converter phase terminal voltage at  $V_{dc}/2$ , 0, and  $-V_{dc}/2$ , respectively. The switching states for x phase are summarized in Table I [11].

TABLE I. THE CONVERTER SWITCHING STATES OF PHASE X

$S_x$	$S_{xI}$	$S_{x2}$	$S_{x3}$	$S_{x4}$	$V_{xo}$
+	1	1	0	0	$V_{dc}/2$
0	0	1	1	0	0
-	0	0	1	1	$-V_{dc}/2$

# B. DC-link Capacitor Models

To describe the dynamics of the voltage across the two dclink capacitors [11], the differential equation is applied as follows

$$\frac{dv_{c1}}{dt} = \frac{i_{c1}}{C_1} \tag{3}$$

$$\frac{dv_{c2}}{dt} = \frac{i_{c2}}{C_2} \tag{4}$$

 $C_1$ ,  $C_2$  upper and lower dc-link capacitors;

 $v_{c1}$ ,  $v_{c2}$  dc-link capacitor voltages;

 $i_{c1}$ ,  $i_{c2}$  currents through  $C_1$  and  $C_2$ , respectively.

Then, using Euler forward approximation method, the discrete-time dc-link model can be obtained as

$$v_{c1}(k+1) = v_{c1}(k) + \frac{i_{c1}(k) T_s}{C_1}$$
 (5)

$$v_{c2}(k+1) = v_{c2}(k) + \frac{i_{c2}(k) T_s}{C_2}$$
 (6)

where  $T_s$  is the sampling period, k and k + 1 represent two consecutive control iterations.

The currents flowing through the dc-link capacitors, i.e.,  $i_{c1}$  and  $i_{c2}$ , are calculated based on the measured instantaneous three-phase grid currents as well as the switching states as [11]

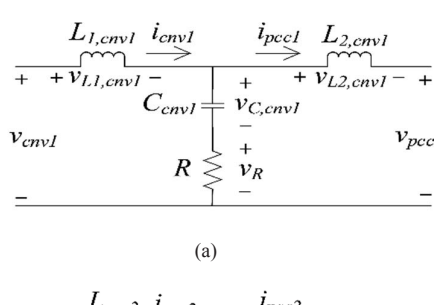
$$i_{c1}(k) = i_{dc}(k) - H_{1a}i_{a}(k) - H_{1b}i_{b}(k) - H_{1c}i_{c}(k)$$
 (7)

$$i_{c2}(k) = i_{dc}(k) + H_{2a}i_a(k) + H_{2b}i_b(k) + H_{2c}i_c(k)$$
 (8)

where  $H_{1x} = 1$  if  $S_x = "+"$ , otherwise  $H_{1x} = 0$ ;  $H_{2x} = 1$  if  $S_x = "-"$ , otherwise  $H_{2x} = 0$ .

#### C. LCL- and LC Filter Models

The *LCL*- and *LC* filter models can be determined by applying KVL and KCL on the one-line diagrams that are shown in Fig. 3. The continuous-time state-space system of the *LCL* filter is derived and explained in (9), whereas (10) presents the continuous-time state-space system of the *LC* filter [5]. Then, the discrete-time mathematical models of *LCL*- and *LC* filters are obtained by applying Euler forward approximation approach and expressed in (11) and (12).



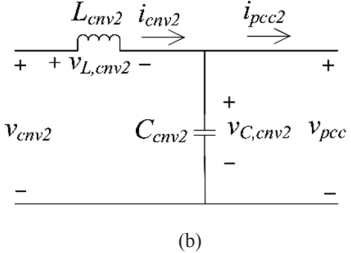


Fig. 3. The one-line diagram of (a) LCL filter and (b) LC filter

$$\frac{dx_1}{dt} = A_1 x_1 + B_1 u_1 \tag{9}$$

where

where

$$x_{1} = \begin{bmatrix} i_{cmv1} \\ i_{pcc1} \\ v_{cap1} \end{bmatrix}, A_{1} = \begin{bmatrix} -R/L_{1,cmv1} & R/L_{1,cmv1} & -1/L_{1,cmv1} \\ R/L_{2,cmv1} & -R/L_{2,cmv1} & 1/L_{2,cmv1} \\ 1/C_{cmv1} & -1/C_{cmv1} & 0 \end{bmatrix}$$

$$u_{1} = \begin{bmatrix} v_{cnv1} \\ v_{pcc} \end{bmatrix}, B_{1} = \begin{bmatrix} 1 / L_{1,cnv1} & 0 \\ 0 & -1 / L_{2,cnv1} \\ 0 & 0 \end{bmatrix}$$

$$\frac{dx_2}{dt} = A_2 x_2 + B_2 u_2 \tag{10}$$

where

$$x_{2} = \begin{bmatrix} i_{cnv2} \\ v_{pcc} \end{bmatrix}, A_{2} = \begin{bmatrix} 0 & -1/L_{cnv2} \\ 1/C_{cnv2} & 0 \end{bmatrix}$$

$$u_{2} = \begin{bmatrix} v_{cnv2} \\ i_{pcc2} \end{bmatrix}, B_{2} = \begin{bmatrix} 1/L_{cnv2} & 0 \\ 0 & -1/C_{cnv2} \end{bmatrix}$$

where

 $L_{1,cnv1}$ ,  $C_{cnv1}$ , R,  $L_{2,cnv1}$  LCL filter parameters; output voltage of solar inverter; i $c_{cnv1}$  solar inverter side current;  $L_{cnv2}$ ,  $C_{cnv2}$  LCL filter output current;  $L_{cnv2}$ ,  $C_{cnv2}$  output voltage of ESS inverter; i $c_{cnv2}$   $c_{cnv2}$ 

# III. THE PROPOSED MODEL PREDICTIVE DROOP CONTROL

Fig. 4 shows the block diagram of the proposed MPDC implemented in the nominal MG. The two main controllers that forms MPDC, i.e., MPC and droop control, are separately explained in this section.

#### A. MPC

Although the MPC has been adopted to control both converters used in the system under investigation, the objectives of the designed controllers are different. To be more specific, the solar inverter output current is controlled to ensure maximum power delivery to the load, i.e., the solar inverter is controlled as a grid-feeding converter. On the other hand, the ESS inverter is controlled as a grid-supporting converter which not only establishes the grid voltage and frequency in islanded modes, but also provides power support to the PCC if needed.

By adopting the algorithm that is illustrated in Fig. 5(a), model predictive current control (MPCC) is proposed to control the solar inverter output current. The solar inverter side current,  $i_{cnv1}$ , and the grid side current,  $i_{pcc1}$ , are measured at sampling instant k. The voltage across the LCL-filter capacitor,  $v_{cnv2,C}$ , is estimated using (11) also at sampling instant k. Then, the current can be predicted for the sampling instant k + 1 by using (11). Finally, the MPCC designed cost function,  $g_I$ , is presented in (13). It is worth noting that, since the sampling time  $T_s$  of the reference current  $i^*_{a\beta}$  is small compared to the fundamental period, it can be assumed that the value of  $i^*_{a\beta}$  remains the same over  $T_s$ , which means that there is no need for the reference current extrapolation [12].

$$g_{1} = \lambda_{1} (i_{\alpha}^{*} - i_{\alpha}^{p})^{2} + \lambda_{1} (i_{\beta}^{*} - i_{\beta}^{p})^{2} + \lambda_{2} (v_{cov1,c1}^{p} - v_{cov1,c2}^{p})$$
(13)

where

 $i^*_{\alpha}, i^*_{\beta}$  real and imaginary parts of the reference current;

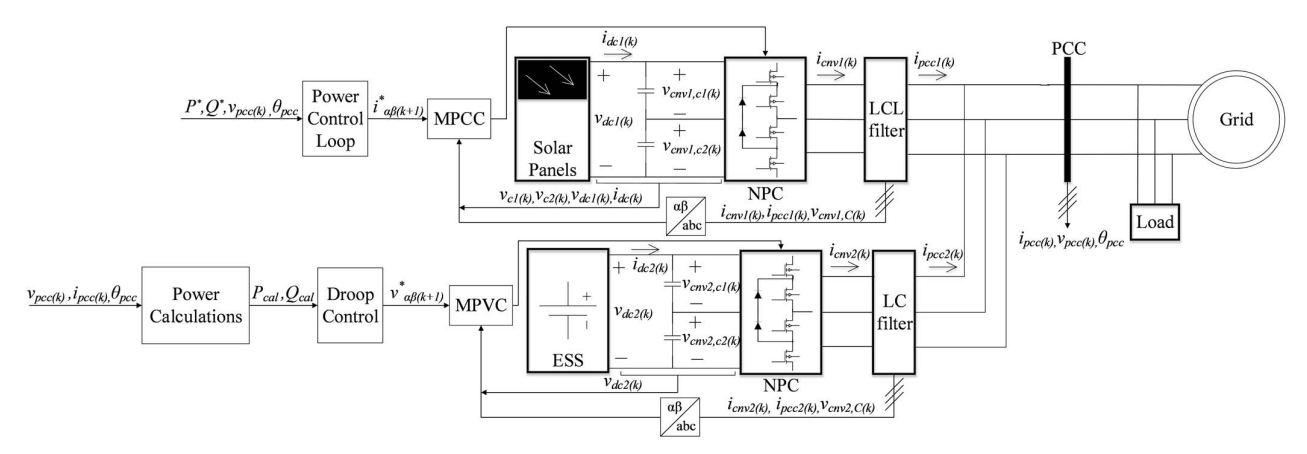


Fig. 4. The proposed model predictive droop control (MPDC)

$$\begin{bmatrix} i_{cm^{2}}(k+1) \\ i_{pcc^{2}}(k+1) \\ v_{cap^{2}}(k+1) \end{bmatrix} = \begin{bmatrix} 1 - RT_{s} / L_{1,cm^{1}} & RT_{s} / L_{1,cm^{1}} & -T_{s} / L_{1,cm^{1}} \\ RT_{s} / L_{2,cm^{1}} & -RT_{s} / L_{2,cm^{1}} & T_{s} / L_{2,cm^{1}} \\ T_{s} / C_{cm^{1}} & -T_{s} / C_{cm^{1}} & 1 \end{bmatrix} \begin{bmatrix} i_{cm^{2}}(k) \\ i_{pcc^{2}}(k) \\ v_{cap^{2}}(k) \end{bmatrix} + \begin{bmatrix} T_{s} / L_{1,cm^{1}} & 0 \\ 0 & -T_{s} / L_{2,cm^{1}} \\ 0 & 0 \end{bmatrix} \begin{bmatrix} v_{cm^{2}}(k) \\ v_{pcc}(k) \end{bmatrix}$$

$$\begin{bmatrix} v_{cm^{2}}(k) \\ v_{cap^{2}}(k) \end{bmatrix}$$

$$\begin{bmatrix} i_{cmv2}(k+1) \\ v_{pcc}(k+1) \end{bmatrix} = \begin{bmatrix} 1 & -T_s / L_{cmv2} \\ T_s / C_{cmv2} & 1 \end{bmatrix} \begin{bmatrix} i_{cmv2}(k) \\ v_{pcc}(k) \end{bmatrix} + \begin{bmatrix} T_s / L_{cmv2} & 0 \\ 0 & -T_s / C_{cmv2} \end{bmatrix} \begin{bmatrix} v_{cmv2}(k) \\ i_{pcc}(k) \end{bmatrix}$$
(12)

 $i^p{}_{\alpha}$ ,  $i^p{}_{\beta}$  real and imaginary parts of the predicted current;  $v^p{}_{cnv1,c1}$ ,  $v^p{}_{cnv1,c2}$  the solar inverter dc-link capacitor voltages;  $\lambda_1, \lambda_2$  weighting factors.

In regard to the ESS inverter, model predictive voltage control (MPVC) is developed following the algorithm shown in Fig. 5(b). The converter side current,  $i_{cmv2}$ , LC filter capacitor voltage,  $v_{cmv2,C}$ , and the grid side current,  $i_{pcc2}$ , are measured at sampling instant k. Using (12), the voltage at the PCC,  $v_{pcc}$ , is predicted at sampling instant k+1. The designed cost function,  $g_2$ , is shown in (14). Again, using small enough sampling time ( $T_8$ ) eliminates the need for using extrapolation techniques [12].

$$g_{2} = \lambda_{3} (v_{\alpha}^{*} - v_{\alpha}^{p})^{2} + \lambda_{3} (v_{\beta}^{*} - v_{\beta}^{p})^{2} + \lambda_{4} (v_{cm^{2},c1}^{p} - v_{cm^{2},c2}^{p}) (14)$$

where

 $v_{\alpha}^{*}, v_{\beta}^{*}$  real and imaginary parts of the reference voltage; real and imaginary parts of the predicted voltage;

 $v^p_{cmv2,c1}, v^p_{cmv2,c2}$  the ESS inverter dc-link capacitor voltages;

 $\lambda_3$ ,  $\lambda_4$  weighting factors.

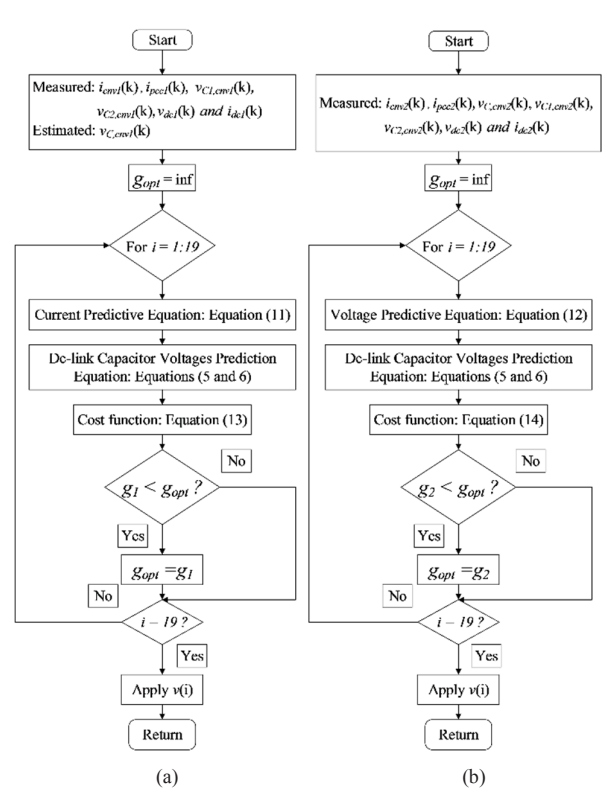


Fig. 5. The flow chart of the proposed (a) MPCC and (b) MPVC.

## B. Droop Control

Droop control allows regulating the voltage and frequency at the PCC for multiple inverters operated in parallel. The grid impedance has considerable influence on the performance of droop control. For a medium voltage (MV) system, similar to the one investigated in this work, the resistive part of the line

impedance can be ignored, since the system is highly inductive. This means the phase difference,  $\delta$ , between the inverter voltage and the PCC voltage is small. Taking into consideration this small power angle, the accuracy of (15) and (16) is not crucially affected if  $\sin(\delta) \approx \delta$  and  $\cos(\delta) \approx 1$  [3], [4], which yields

$$P = \frac{v_{cnv2}}{x} (v_{pcc} \sin \delta) \approx \frac{v_{pcc} v_{cnv2} \delta}{x}$$
 (15)

$$Q = \frac{v_{cnv2}}{x} (v_{cnv2} - v_{pcc} \cos \delta) \approx \frac{v_{cnv2} (v_{cnv2} - v_{pcc})}{x}$$
 (16)

where

P, Q active and reactive power flowing from the NPC to the PCC; the ESS converter terminal voltage;

 $v_{pcc}$  the PCC voltage; x line inductance;

 $\delta$  phase difference between  $v_{cnv2}$  and  $v_{pcc}$ .

From (15) and (16), it can be concluded that the frequency and voltage at the PCC can be regulated by P and Q, respectively. The droop control equations, therefore, can be expressed as

$$\omega = \omega_0 - k_{p} (P - P_0) \tag{17}$$

$$V = V_0 - k_a (Q - Q_0)$$
 (18)

where

 $\omega_0$ ,  $V_0$  reference frequency and voltage;  $\omega$ , V PCC frequency and voltage;  $P_0$ ,  $Q_0$  reference active and reactive power;  $k_p$ ,  $k_q$  droop coefficients.

#### IV. SIMULATION STUDIES

Simulation studies have been performed to validate the effectiveness of the proposed MPC algorithms and the performance of the MG system under different operating modes. The results, which are summarized in Figs. 6 and 7, clearly show the enhancement of using MPC to improve the response of droop control against the variations of solar irradiance.

## A. Simulation Results for Grid-tied Operating Mode

When operated in grid-connected operating mode, the solar inverter is synchronized and connected to the PCC, where a 242 kW local load is tied. In this case, only the solar inverter is contributing power to the PCC. The corresponding simulation results are shown in Fig. 6. The maximum power, that the solar inverter can produce, is 236 kW when solar irradiance is  $1000 \text{ W/}m^2$ . The three-phase line-to-neutral voltage at the PCC, as depicted in Fig. 6(a), remained balanced and constant at rated 200 V, although the solar irradiance, shown in Fig. 6(f), significantly dropped and increased at t =2.0 s and t = 3.0 s, respectively. In addition, the PCC's frequency, presented in Fig. 6(e), is slightly affected by these changes in solar irradiance. Figures 6(b) and (c) demonstrate the three-phase currents of solar inverter and the grid, respectively. The overall current, consumed by the load, is presented in Fig. 6(d). The high dynamic response and perfect reference tracking of MPC can be clearly seen in Fig. 6(g) where the actual current tracks its reference as the solar irradiance dramatically changed. Fig. 6(h) shows the variation of the power generated by the solar converter due to the changing of the atmospheric condition.

#### B. Simulation Results for Stand-alone Operating Mode

The study in stand-alone operating mode also shows the effectiveness and robustness of the proposed MPC when the main power supply does not provide support to the microgrid. In other words, the three-phase voltage and frequency at the

PCC are established by the ESS since the main grid is disconnected. The results from this case are summarized and presented in Fig. 7 considering similar ambient condition as in grid-connected operating mode. As it is indicated in Figs. 7(a) and (e), the three-phase voltage and frequency at the PCC are not impacted by the irradiance changes. The three-phase currents generated by the ESS inverter and solar inverter are depicted in Figs. 7(b) and (c), whereas Fig. 7(d)

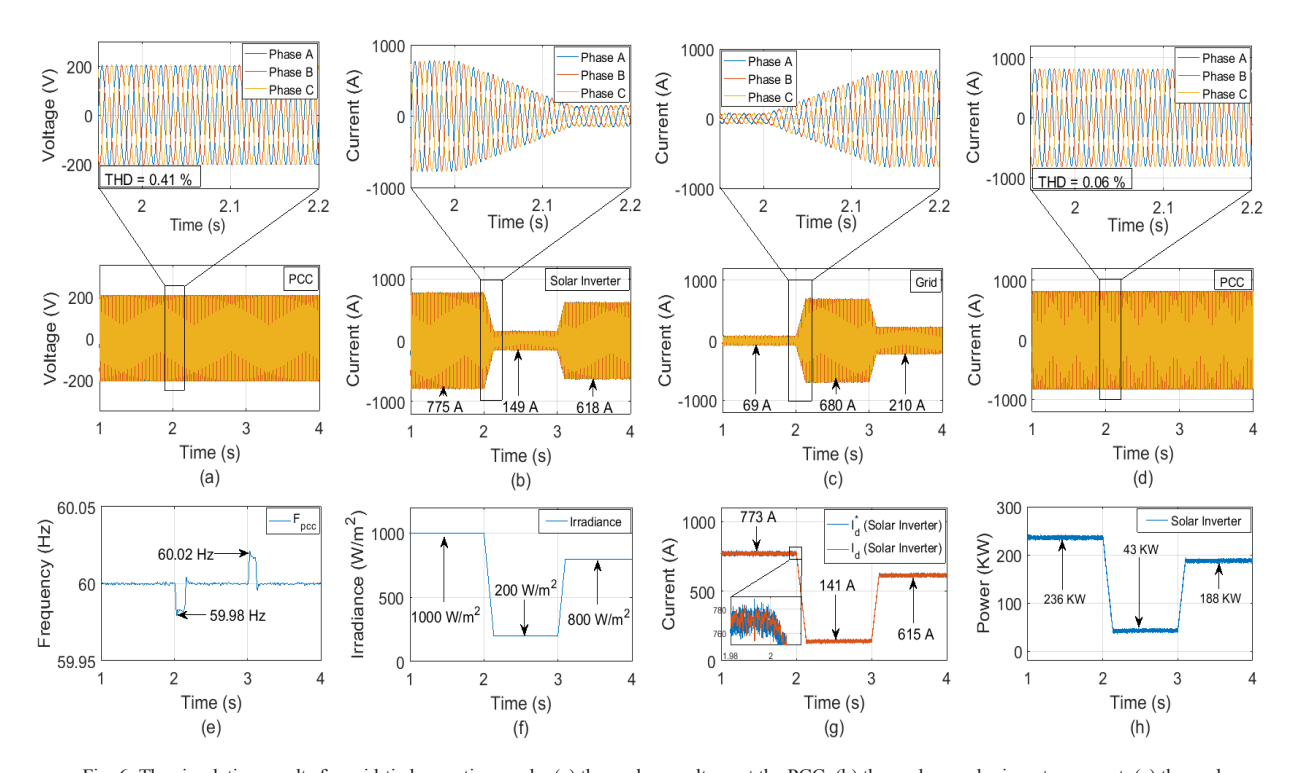


Fig. 6. The simulation results for grid-tied operating mode: (a) three-phase voltage at the PCC, (b) three-phase solar inverter current, (c) three-phase grid current, (d) three-phase current at the PCC, (e) frequency at the PCC, (f) iradiance applied to the solar inverter, (g) reference and actual currents of the solar inverter in dq0 frame, and (h) active power delivered by the solar converter to the PCC

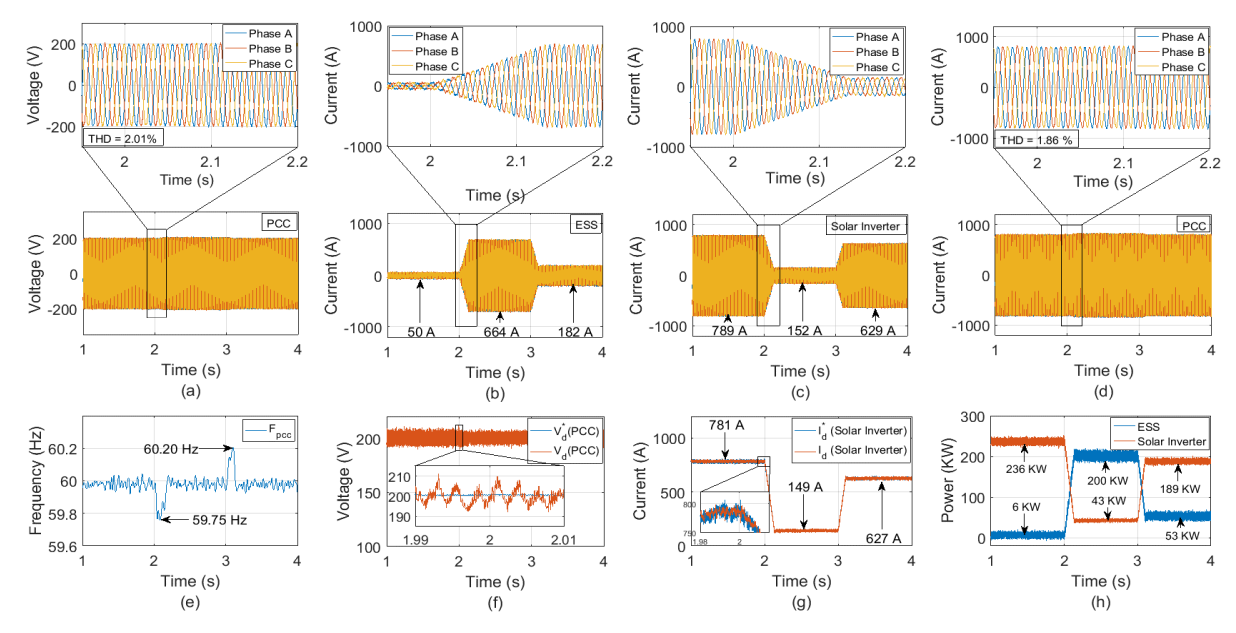


Fig. 7. Simulation results for stand-alone operating mode: (a) three-phase voltage at the PCC, (b) three-phase ESS inverter current, (c) three-phase solar inverter current, (d) three-phase current at the PCC, (e) frequency at the PCC, (f) reference and actual voltages of the ESS inverter in dq0 frame, (g) reference and actual currents of the solar inverter in dq0 frame, and (h) active power delivered by the ESS inverter and solar converter to the PCC.

presents the current withdrawn by the load linked to the PCC. The fast-tracking performance can be clearly observed in Figs. 7(f) and (g), where the voltage and current are tracking their references by means of MPDC. The simulated power delivered by each converter is demonstrated in Fig. 7(h). For any drop or increase in the power generated by the solar inverter, the ESS converter is controlled to compensate for these sudden changes so that the voltage and frequency remain constant at the PCC.

#### V. EXPERIMENTAL RESULTS

In this work, in addition to the simulation studies, controller HIL (C-HIL) studies are performed to validate the effectiveness of the proposed MPDC. It is worth noting that the experimental results match the simulation results, which further validates the effectiveness of the proposed control method.

## A. Experimental Results for Grid-tied Operating Mode

Fig. 8 shows the voltage at the PCC, while the PCC frequency is presented in Fig. 12(a). Though the irradiance is changing considerably over time, the three-phase voltage and frequency at the PCC remained not affected. Additionally, the three-phase current drawn by the load at the PCC is presented in Fig. 9. The three-phase solar inverter current, shown in Fig. 10, remained balanced regardless solar irradiance variations. Fig. 11 validates the high performance tracking as the solar inverter actual current is tracking the reference current. The power generated by the solar inverter, proportionally related to the solar irradiance variations, is presented in Fig. 12(b).

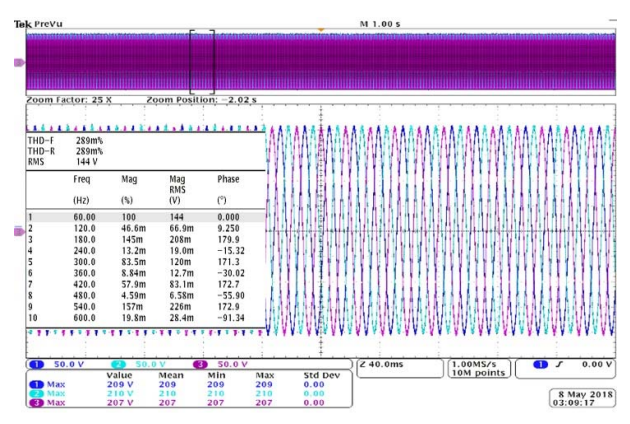


Fig. 8. Voltage at the PCC (grid-tied mode).

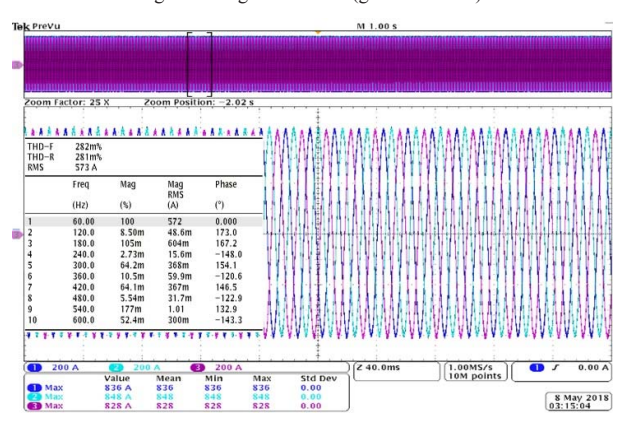


Fig. 9. Current at the PCC (grid-tied mode).

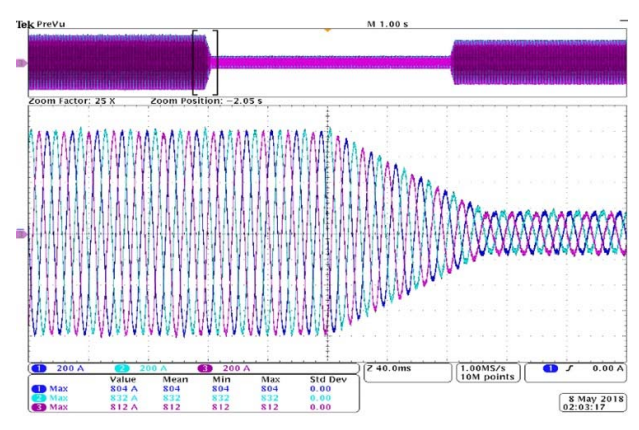


Fig. 10. Solar inverter current at the PCC (grid-tied mode).

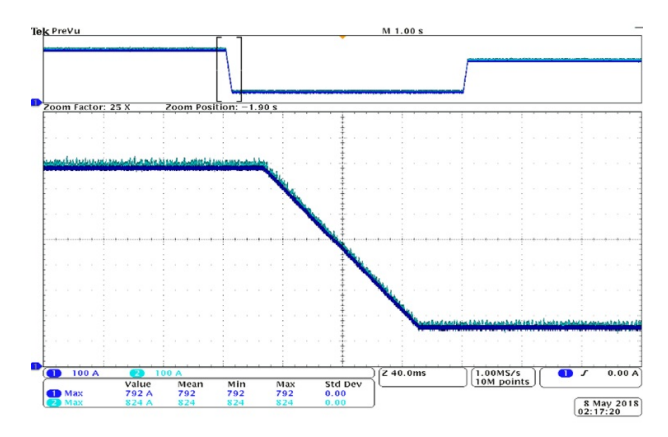


Fig. 11. Reference and actual currents of the solar inverter (grid-tied mode).

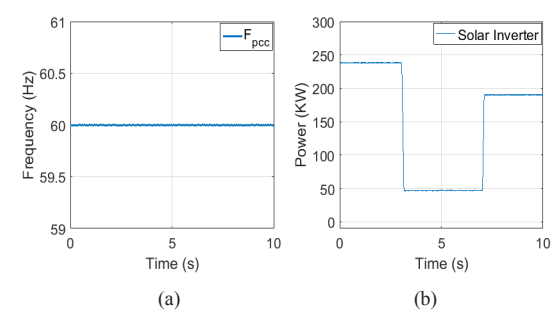


Fig. 12. (a) frequency at the PCC and (b) power supplied by solar inverter (grid-tied mode).

## B. Experimental Results for Stand-alone Operating Mode

The designed controller has also been proven to be functional and effective in the islanded mode. The fast irradiance changes have light impact on the three-phase voltage and current at the PCC as shown in Figs. 13 and 14, similar for the PCC's frequency, as shown in Fig. 19(a). The three-phase ESS inverter and solar inverter currents are illustrated in Figs. 15 and 16. For any drop in solar irradiance, the ESS inverter can always provide current to meet the load demand. Furthermore, the fast dynamic response and the effectiveness of MPDC are illustrated in Figs. 17 and 18, where the solar inverter current and ESS voltage well track their references. Fig 19(b) presents the power supplied by both ESS inverter as well as the solar inverter.

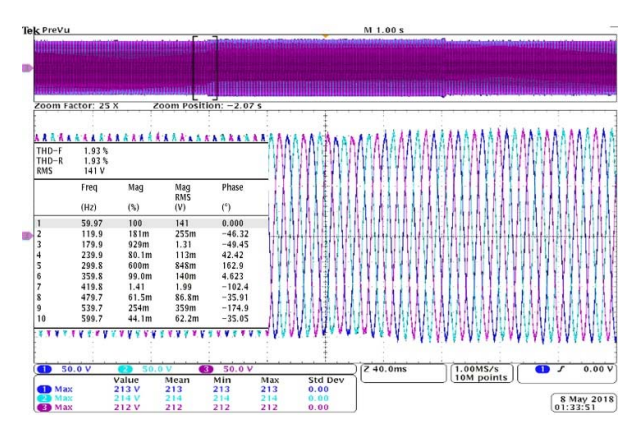


Fig. 13. Voltage at the PCC (stand-alone mode).

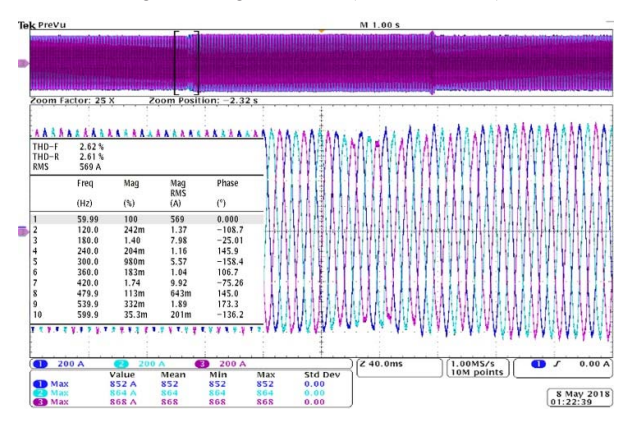


Fig. 14. Current at the PCC (stand-alone mode).

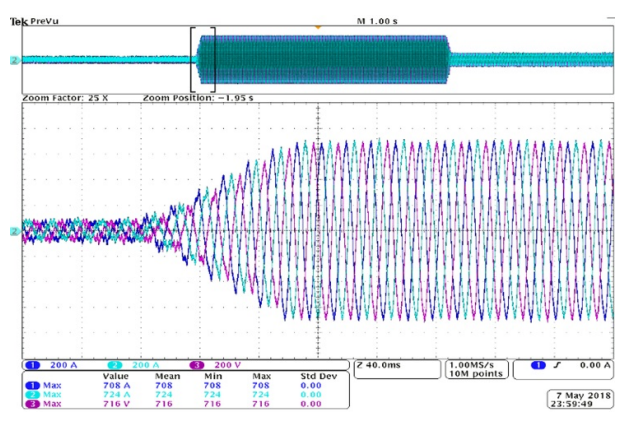


Fig. 15. ESS inverter current (stand-alone mode).

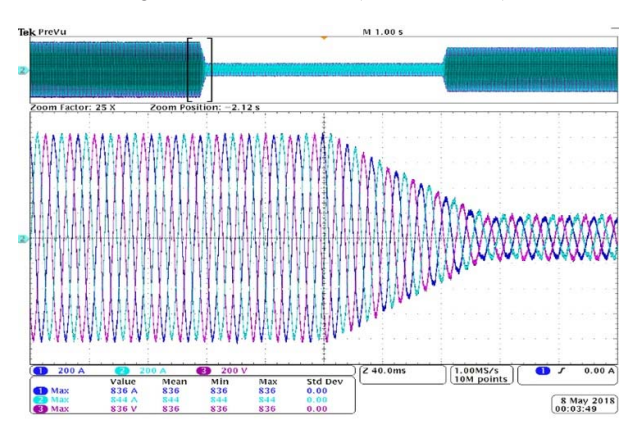


Fig. 16. Solar inverter current (stand-alone mode).

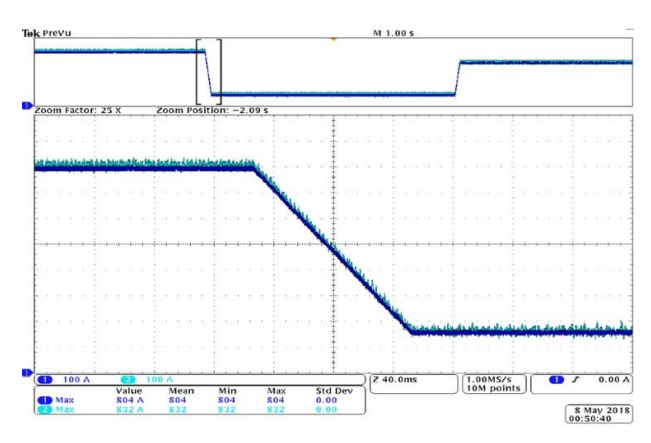


Fig. 17. Reference and actual currents of the solar inverter (stand-alone mode).

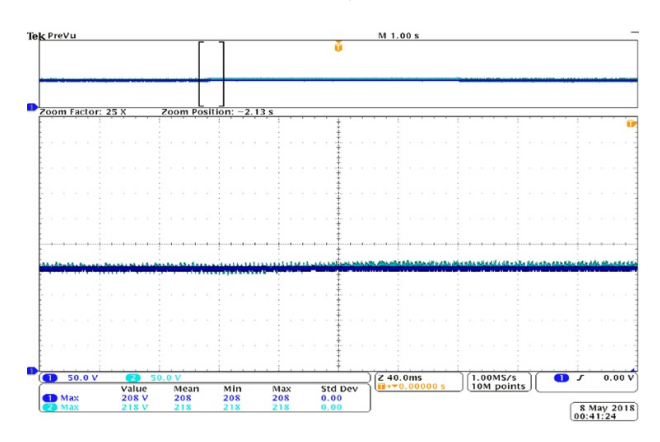


Fig. 18. Reference and actual voltages of the ESS inverter (stand-alone mode).

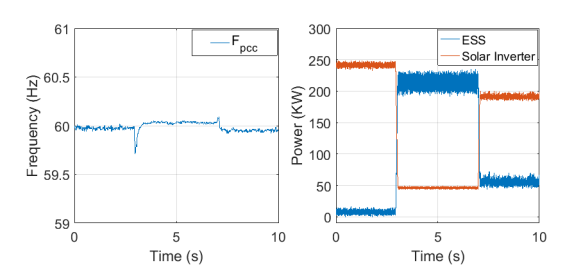


Fig. 19. (a) frequency at the PCC and (b) power generated by the ESS and solar inverter (stand-alone mode).

## VI. CONCLUSIONS

In this work, a novel MPC framework is proposed for DER converters, including a solar inverter and an ESS inverter, feeding a critical load in a microgrid under different operating modes. More specifically, a MPC is proposed to control the solar inverter in grid-tied operating modes, while a MPDC controlled solar inverter is demonstrated to work in standalone operating modes when the ESS is also connected to the system. Due to its fast dynamic response, the proposed MPC and MPDC have demonstrated their capabilities to handle the fast changing ambient condition. Simulation results using Matlab/Simulink have been presented to verify the ability of MPDC to work under various scenarios. Comprehensive description and validation for the proposed MPDC using HIL are also presented in this paper.

#### REFERENCES

- [1] J. Rocabert, A. Luna, F. Blaabjerg and P. Rodríguez, "Control of Power Converters in AC Microgrids," in *IEEE Transactions on Power Electronics*, vol. 27, no. 11, pp. 4734-4749, Nov. 2012.
- [2] X. Li, H. Zhang, M. B. Shadmand and R. S. Balog, "Model Predictive Control of a Voltage-Source Inverter With Seamless Transition Between Islanded and Grid-Connected Operations," in *IEEE Transactions on Industrial Electronics*, vol. 64, no. 10, pp. 7906-7918, Oct. 2017.
- [3] J. M. Guerrero, L. Hang and J. Uceda, "Control of Distributed Uninterruptible Power Supply Systems," in *IEEE Transactions on Industrial Electronics*, vol. 55, no. 8, pp. 2845-2859, Aug. 2008.
- [4] J. M. Guerrero, J. C. Vasquez, J. Matas, L. G. de Vicuna and M. Castilla, "Hierarchical Control of Droop-Controlled AC and DC Microgrids—A General Approach Toward Standardization," in *IEEE Transactions on Industrial Electronics*, vol. 58, no. 1, pp. 158-172, Jan. 2011.
- [5] S. Wang, Z. Liu, J. Liu, R. An and M. Xin, "Breaking the boundary: A droop and master-slave hybrid control strategy for parallel inverters in islanded microgrids," 2017 IEEE Energy Conversion Congress and Exposition (ECCE), Cincinnati, OH, 2017, pp. 3345-3352
- [6] T. Dragičević, "Model Predictive Control of Power Converters for Robust and Fast Operation of AC Microgrids," in *IEEE Transactions* on *Power Electronics*, vol. 33 PP, no. 7, pp. 6304-6317, July 2018.

- [7] J. Rodriguez et al., "Predictive Current Control of a Voltage Source Inverter," in *IEEE Transactions on Industrial Electronics*, vol. 54, no. 1, pp. 495-503, Feb. 2007.
- [8] S. Kouro, P. Cortes, R. Vargas, U. Ammann and J. Rodriguez, "Model Predictive Control—A Simple and Powerful Method to Control Power Converters," in *IEEE Transactions on Industrial Electronics*, vol. 56, no. 6, pp. 1826-1838, June 2009.
- [9] P. Acuña, L. Morán, M. Rivera, J. Dixon and J. Rodriguez, "Improved Active Power Filter Performance for Renewable Power Generation Systems," in *IEEE Transactions on Power Electronics*, vol. 29, no. 2, pp. 687-694, Feb. 2014.
- [10] M. Siami, D. A. Khaburi, A. Abbaszadeh and J. Rodríguez, "Robustness Improvement of Predictive Current Control Using Prediction Error Correction for Permanent-Magnet Synchronous Machines," in *IEEE Transactions on Industrial Electronics*, vol. 63, no. 6, pp. 3458-3466, June 2016.
- [11] J. Rodriguez and P. Cortes, Predictive Control of Power Converters and Electrical Drives, 1st ed., 2012, John Wiley & Sons, Ltd.
- [12] A. Calle-Prado, S. Alepuz, J. Bordonau, J. Nicolas-Apruzzese, P. Cortés and J. Rodriguez, "Model Predictive Current Control of Grid-Connected Neutral-Point-Clamped Converters to Meet Low-Voltage Ride-Through Requirements," in *IEEE Transactions on Industrial Electronics*, vol. 62, no. 3, pp. 1503-1514, March 2015.